Precise calibration of cavity forward and reflected signals using low-level radio-frequency system[*]

Jin-Ying Ma,[1] Feng Qiu,[1,2,†] Long-Bo Shi,[1] Zheng-Long Zhu,[1] Tian-Cai Jiang,[1] Zong-Heng Xue,[1] Ke-An Jin,[1] Qi Chen,[1] Cheng-Ye Xu,[1] Xing-Hao Ding,[2] Zheng Gao,[1] Lie-Peng Sun,[1,2] Gui-Rong Huang,[1,2] and Yuan He[1,2]

[1]*Institute of Modern Physics, Chinese Academy of Sciences, Lanzhou 730000, China*
[2]*School of Nuclear Science and Technology, University of Chinese Academy of Sciences, Beijing 100049, China*

Precise measurements of the cavity forward (V_f) and reflected signals (V_r) are essential for characterizing other key parameters such as the cavity detuning and forward power. In practice, it is challenging to measure V_f and V_r precisely because of crosstalk between the forward and reflected channels (e.g., coupling between the cavity reflected and forward signals in a directional coupler with limited directivity). For DESY, a method based on the cavity differential equation was proposed to precisely calibrate the actual V_f and V_r. In this study, we verified the validity and practicability of this approach for the Chinese ADS front-end demo superconducting linac (CAFe) facility at the Institute of Modern Physics and a compact energy recovery linac (cERL) test machine at KEK. At the CAFe facility, we successfully calibrated the actual V_f signal using this method. The result demonstrated that the directivity of directional couplers might seriously affect the accuracy of V_f measurement. At the cERL facility, we calibrated the Lorentz force detuning (LFD) using the actual V_f. Our study confirmed that the precise calibration of V_f significantly improves the accuracy of the cavity LFD measurement.

Keywords: Forward and reflected signals, Measurement, Calibration

I. INTRODUCTION

The Chinese ADS front-end demo superconducting linac (CAFe) was constructed at the Institute of Modern Physics to develop the key technologies for a superconducting (SC) front-end linac. It was used to demonstrate the possibility of a 10 mA high-power continuous-wave (CW) proton beam for the China Initiative Accelerator-Driven System project [1–3]. The CAFe facility is a 162.5 MHz SC radio frequency (RF) facility operating in CW mode and consists of a normal conducting section and an SC section. As shown in Fig. 1, the normal conducting section is composed of an ion source, low-energy beam transport line (LEBT), RF quadrupole accelerator, and medium-energy beam transport line (MEBT). The SC section is composed of SC accelerating units, which consist of 23 SC half-wave resonator cavities and are assembled in four cryomodules (CM1 to CM4).

The cavity forward and reflected signals (V_f and V_r) are typically used to control other key parameters such as the cavity voltage signal (V_c), cavity detuning (Δf), and forward power. For example, at the SC test facility (STF) at KEK [4], because there is no pickup antenna in the STF RF gun cavity, V_c is reconstructed by computing the superposition of V_f and V_r ($V_c = V_f + V_r$) [5]. Note that in this paper, V_c, V_f, and V_r refer to baseband signals, which can be represented by their amplitude and phase (e.g., $V_c = |V_c|e^{j\angle V_c}$). The cavity pickup signal at the Paul Scherrer Institute was found to be corrupted by noise [6]. Therefore, V_c was recalculated using the actual V_f and V_r, and the noise was successfully removed. In addition, V_f measurement can affect the accuracy of the cavity dynamical detuning. For instance, at the compact energy recovery linac (cERL) test facility at KEK, we compared the cavity Lorentz force detuning (LFD, Δf_{LFD}) calculated

using the cavity differential equation with that calibrated using the square of the accelerating gradient. We found that the results of these two methods do not agree at the beginning of cavity filling. This discrepancy was attributed to the inaccuracy of V_f measurement, which was caused by the limited directivity of the RF directional coupler [7].

At CAFe, we measured the V_c, V_f, and V_r signals and the low-level RF (LLRF) output in cavity CM_{3-5} (see Fig. 2). The location of the LLRF output signal is marked in Fig. 3. The cavity amplitude loop was operated in closed-loop mode, whereas the phase loop was operated in open-loop mode. As shown in Fig. 2, the cavity amplitude error was well compensated by the feedback loop. By contrast, because the phase loop was open, the cavity phase fluctuated greatly owing to perturbations such as microphonics and Δf_{LFD}. Moreover, Fig. 2 shows that there is a significant difference between the V_f phase and LLRF output phase. One possible reason for the phase difference is the nonlinearity of the solid-state amplifier (SSA). Another possible reason involves the inaccurate measurement of V_f owing to crosstalk between the forward and reflected channels, for example, coupling between the cavity reflected and forward signals in the directional coupler. Later sections of this article demonstrate that the nonlinearity of the SSA is not the primary reason for this phase difference.

Because of crosstalk between the measurement channels, the measured V_f signal is mixed with the V_r signal, resulting in inaccurate V_f measurement. To address this problem, Brandt proposed a method of eliminating the effect of V_r on the V_f signal [8]. We calibrated the actual value of V_f in CM_{3-5} at CAFe and in an SC cavity at KEK-cERL using this method. The measurement results confirmed that this method is effective.

The remainder of this paper is organized as follows. Section II briefly describes the CAFe LLRF system. Section III reviews the algorithms used to calibrate the actual values of V_f and V_r. In addition, the actual V_f and V_r values are estimated with higher precision. Section IV demonstrates the validity of the method using the experimental results for CAFe

---

and cERL. Section V presents a discussion of our future work. Finally, we summarize our study in Sec. VI.

II. LLRF SYSTEM

At CAFe, the LLRF data acquisition system is used to measure the amplitude, phase, and frequency and then use various signal processing methods to monitor and control the RF fields. Figure 3 shows a simplified illustration of the layout of the digital LLRF system at CAFe. The frequencies of the RF signals and the intermediate frequency (IF) signal are 162.5 and 25 MHz, respectively. A field-programmable gate array (FPGA) module is used for real-time signal processing and high-speed data acquisition. RF signals such as V_c, V_f, and V_r are first converted to IF signals. The IF signals are sampled at 100 MHz via a 16-bit analog-to-digital converter (ADC) and are fed to the FPGA. Then, the amplitude and phase of V_c are extracted from the IF signals. Subsequently, the amplitude and phase signals are compared with their setpoints, and their errors are calculated. These error signals are controlled by a proportional and integral (PI) controller. The controlled amplitude and phase signals are used to rebuild the IF signal. Next, the IF signal is up-converted, and the up-converted signal is used to drive the SSA and ultimately power the cavity. An ARM chip is integrated into the FPGA. An experimental physics and industrial control system (EPICS) is installed on the ARM chip as an embedded Linux system for data acquisition. The amplitude and phase waveforms of V_c, V_f, and V_r are saved to the hard drive of the CPU controller during measurement, and the measurement data are analyzed offline.

III. CALIBRATION OF REAL CAVITY FORWARD SIGNAL

To calibrate the real V_f and V_r signals (see Fig. 2), we review the method of Brandt and present an example for cavity CM_{3-5} at CAFe. CM_{3-5} is mounted in the third cryomodule (CM_3). It is the fifth cavity in CM_3, and the loaded quality factor is 3.8×10^5, as illustrated in Fig. 1.

Figure 4 shows the V_c, V_f, and V_r signals measured by the LLRF system during the pulse conditioning of cavity CM_{3-5}. According to these results, the cavity signal cannot be obtained by computing the measured signal between the V_f^* and V_r^* vectors if the two signals are uncalibrated. The actual cavity signal V_c is a superposition of the actual V_f and V_r signals, and it can be reconstructed using the formula [8–10]

$$V_c = V_f + V_r. \tag{1}$$

The actual V_f and V_r signals can be calibrated using the measured cavity forward and reflected signals according to [5, 8]

$$\begin{bmatrix} V_f \\ V_r \end{bmatrix} = \begin{bmatrix} a & b \\ c & d \end{bmatrix} \begin{bmatrix} V_f^* \\ V_r^* \end{bmatrix}, \tag{2}$$

where V_f^* and V_r^* are the measured values. In this equation, a, b, c, and d are complex constants related to the actual and measured values. Then, Eq. (1) can be written as

$$V_c = X V_f^* + Y V_r^*, \tag{3}$$

where $X = a + c$ and $Y = b + d$. The complex constants X and Y can be estimated by the multiple linear regression method. The specific calculation methods are as follows.

The complex signals V, X, and Y can be written as $V = R(V) + jI(V)$, $X = C_1 + jC_2$, and $Y = C_3 + jC_4$, respectively. $R(V)$, C_1, and C_3 represent the real parts, whereas $I(V)$, C_2, and C_4 represent the imaginary parts. Then, Eq. (3) can be written as

$$R(V_c) + jI(V_c) = (C_1 + jC_2)[R(V_f^*) + jI(V_f^*)] \\ + (C_3 + jC_4)[R(V_r^*) + jI(V_r^*)]. \tag{4}$$

For a single pulse with sampled data points V_{ck}, V_{fk}^*, and V_{rk}^*, where k runs from 1 to n, this method can be used to obtain a linear, overdetermined system of equations. Let V_c be the response variable; then

$$\mathbf{y} = \begin{bmatrix} R(V_{C1}) & \cdots & R(V_{Cn}) & I(V_{C1}) & \cdots & I(V_{Cn}) \end{bmatrix}^T. \tag{5}$$

In addition, let the measured values V_f^* and V_r^* form the regressor matrix

$$\mathbf{A} = \begin{bmatrix} R(V_{f1}^*) & -I(V_{f1}^*) & R(V_{r1}^*) & -I(V_{r1}^*) \\ R(V_{f2}^*) & -I(V_{f2}^*) & R(V_{r2}^*) & -I(V_{r2}^*) \\ \vdots & \vdots & \vdots & \vdots \\ R(V_{fn}^*) & -I(V_{fn}^*) & R(V_{rn}^*) & -I(V_{rn}^*) \\ I(V_{f1}^*) & R(V_{f1}^*) & I(V_{r1}^*) & R(V_{r1}^*) \\ I(V_{f2}^*) & R(V_{f2}^*) & I(V_{r2}^*) & R(V_{r2}^*) \\ \vdots & \vdots & \vdots & \vdots \\ I(V_{fn}^*) & R(V_{fn}^*) & I(V_{rn}^*) & R(V_{rn}^*) \end{bmatrix}. \tag{6}$$

Then the relation

$$\mathbf{y} = \mathbf{A}\mathbf{C} \tag{7}$$

is approximately satisfied for some parameter vector

$$\mathbf{C} = \begin{bmatrix} C_1 & C_2 & C_3 & C_4 \end{bmatrix}^T, \tag{8}$$

where $\mathbf{C}$ represents the values of interest. The best estimates of C_1, C_2, C_3, and C_4 can be determined using multiple linear regression. The complex constants X and Y can be obtained using these $\mathbf{C}$ values. The crosstalk elements b can be taken into account using the information from the RF decay time (after 3.5 ms in Fig. 4). During decay, the actual V_f should be 0, and the factors a and b are then limited by another complex factor Z as

$$Z = a/b = -V_r^*/V_f^* \quad (t > 3.5\text{ms}). \tag{9}$$

Then the complex factors can be expressed in terms of X, Y, and Z according to

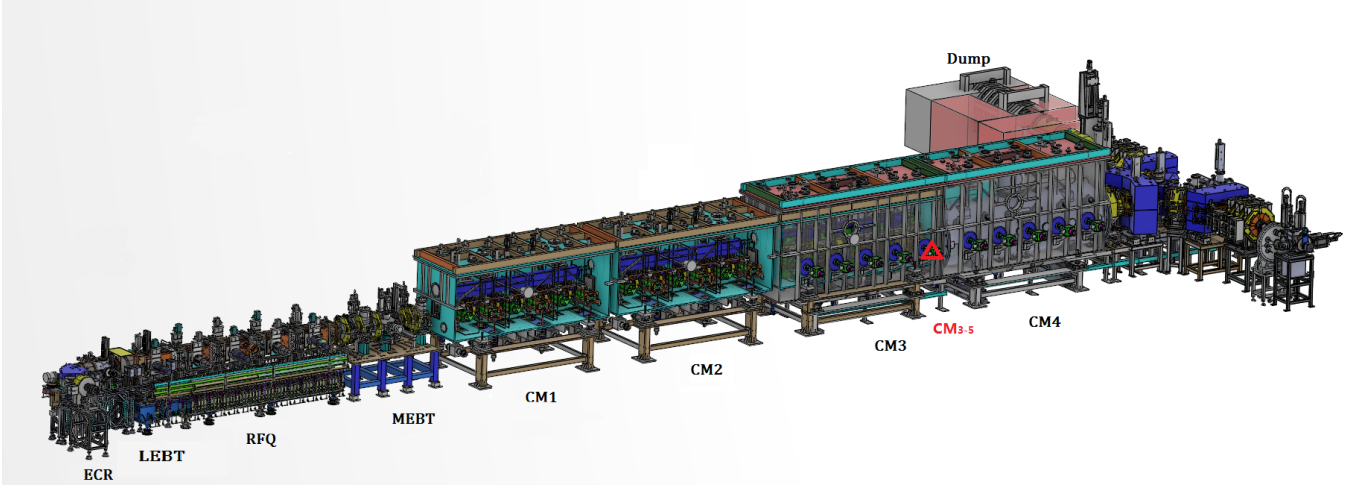$$\begin{cases} a = a \\ b = a/Z \\ c = X - a \\ d = Y - a/Z. \end{cases} \tag{10}$$

Fig. 1. (Color online) Layout of CAFe facility. The half-wave SC cavities are mounted in four cryomodules (CM1 to CM4). Cavity CM_{3-5} is marked by a red triangle.
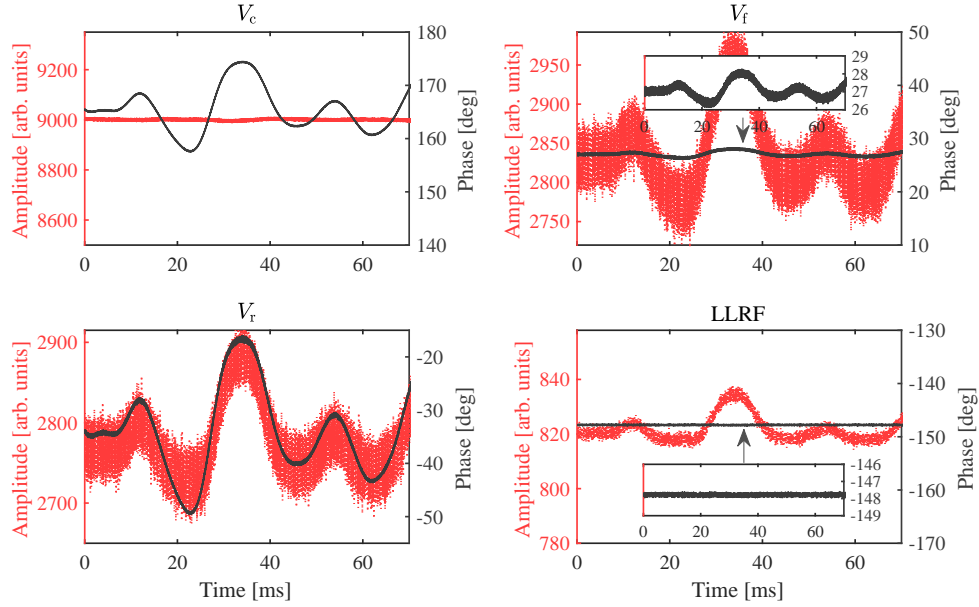

Fig. 2. (Color online) Comparison of amplitude and phase of cavity voltage signal (V_c), cavity forward signal (V_f), cavity reflected signal (V_r), and LLRF output signal. The cavity amplitude loop was operated in closed-loop mode, whereas the phase loop was operated in open-loop mode. Figure shows that the phase of V_f differs from that of the LLRF output.

The final unknown complex factor a can be extracted numerically from the cavity differential equation assuming a constant cavity half-bandwidth $\omega_{0.5}$, which can be estimated in terms of the field decay curve ($t > 3.5$ ms).

The cavity equation can be written in polar coordinates as

$$\frac{\mathrm{d}|V_\mathrm{c}|}{\mathrm{d}t} + |V_\mathrm{c}|\omega_{0.5} = \omega_{0.5} \cdot (2|V_\mathrm{f}|)\cos(\theta - \phi). \tag{11}$$

Consequently, the differential of $|V_\mathrm{c}|$ can be computed using the formula

$$y(a, t_k) = \omega_{0.5}\left[(2|V_\mathrm{f}|)\cos(\theta - \phi) - |V_\mathrm{c}|\right], \tag{12}$$

where θ and ϕ represent the phases of V_c and V_f, respectively. The variable $y(a)$ represents the calibrated $\frac{\mathrm{d}|V_\mathrm{c}|}{\mathrm{d}t}$ as a function of the factor a according to Eq. (13). By contrast, $\frac{\mathrm{d}|V_\mathrm{c}|}{\mathrm{d}t}$ can be directly calibrated from the amplitude of V_c, which is independent of a. The difference between these two calculations should be minimized by optimizing a. Therefore, we denote the difference as $\lambda^2(a)$.

$$\lambda^2(a) = \sum_{t_k}\left[\frac{\mathrm{d}|V_\mathrm{c}|}{\mathrm{d}t} - y(a)\right]^2 \tag{13}$$
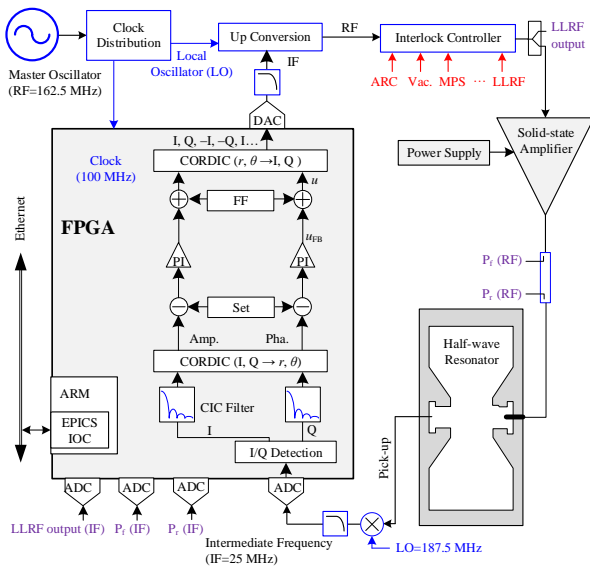
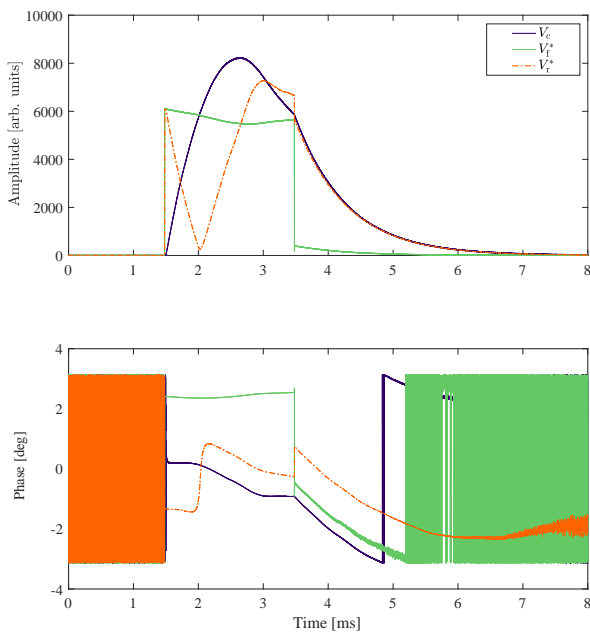Fig. 3. Schematic of digital LLRF system at CAFe. The location of the LLRF output signal is marked.

Fig. 4. (Color online) Measured cavity voltage, forward, and reflected signals in CM_{3-5} during RF commissioning.
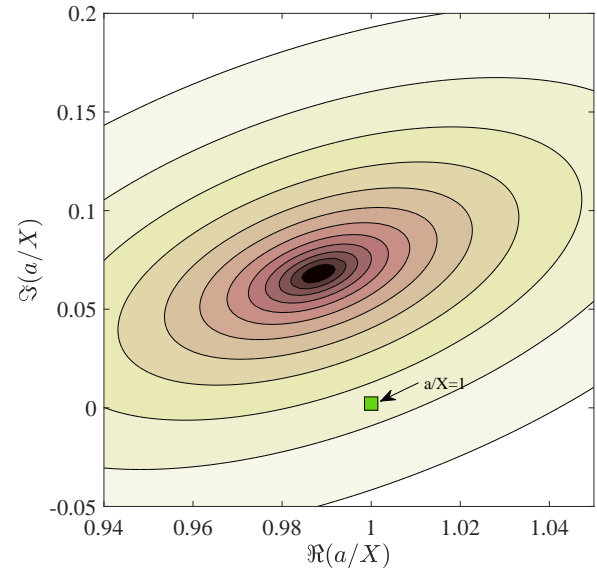

Fig. 5. (Color online) Scanning result of the parameter λ^2. The optimized factor a/X is $0.99 + 0.07i$. The X and Y axes represent the real and imaginary parts of a/X, respectively.
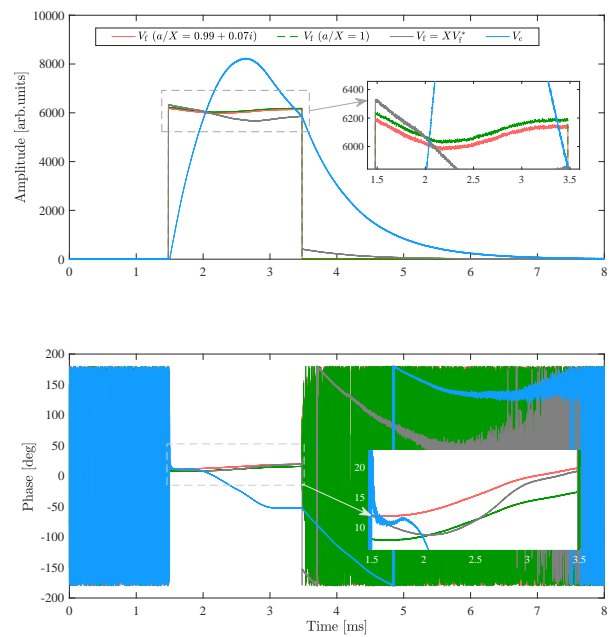

Fig. 6. (Color online) Comparison of cavity forward voltage V_{f} for $a/X = 1$ and $a/X = 0.99 + 0.07i$. The waveforms of XV_{f}^* and V_{c} are also presented for comparison.

Note that a is a complex number with two components. A two-dimensional map can be obtained by sweeping the real and imaginary components of a, as shown in Fig. 5. Here, the color axis represents the value of $\lambda^2(a)$. The X and Y axes represent the real and imaginary components of (a/X), respectively. The optimal value of (a/X) is clearly $0.99 + 0.07i$. To better illustrate this result, Figs. 6 and 7 compare the waveforms of V_{f} and $y(a)$, respectively, for $a/X = 1$ and $a/X = 0.99 + 0.07i$. The difference between $\frac{\mathrm{d}|V_{\mathrm{c}}|}{\mathrm{d}t}$ and y is minimized when the optimal value of a is used.

IV. EXPERIMENTAL VERIFICATION

To demonstrate the method described in the previous section, the V_{f} measurement data were processed and analyzed at the CAFe and cERL facilities.
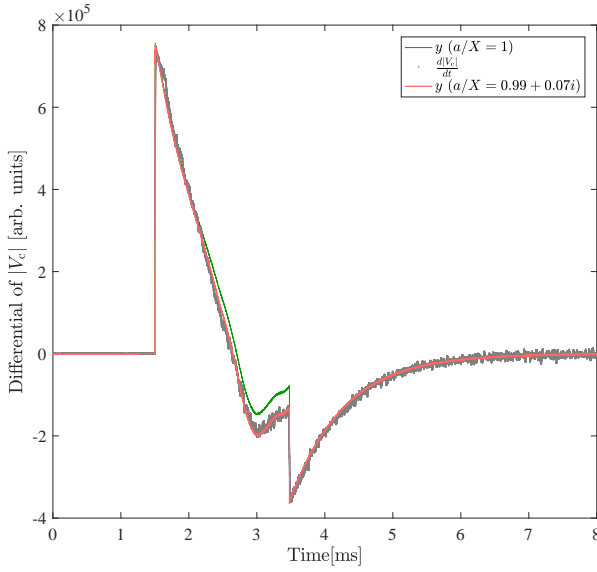
Fig. 7. (Color online) Comparison of parameter y for $a/X = 1$ and $a/X = 0.99 + 0.07i$. The quantity $\frac{\mathrm{d}|V_\mathrm{c}|}{\mathrm{d}t}$ is also plotted as a reference.

A.   Experimental result at CAFe

During the RF commissioning at CAFe, the LLRF output, SSA output, and V_f^* and V_r^* signals of CM_{3-5} were down-converted and sent to the ADCs of the LLRF system. The positions of the four signals (points A, B, C, and D, respectively), are shown in Fig. 8. As mentioned in Sect. I, the phase of V_f^* differs from the LLRF output phase according to the measurement (see Figs. 2 and 9). In theory, the LLRF output phase and V_f phase should be in agreement, whereas the phases at points A and C differ greatly, according to Fig. 9. As shown in Fig. 8, in the ideal case, the phases of the LLRF output (point A) and V_f (point C) should be in agreement. The discrepancy has two possible causes: the nonlinearity of the SSA and crosstalk between the measurement channels (that is, the unwanted coupling of some components of V_r with V_f). We analyze the effects of these two causes as follows.

To eliminate the impact of the nonlinearity of the SSA, we measured the output characteristics of the SSA, as shown in Fig. 10. The amplitude and phase characteristics of the SSA output were measured using a network analyzer. The operating point for Fig. 2 (and Fig. 9) is marked on Fig. 10 as $P(x, y)$. The amplitude nonlinearity curve can be fitted using the polynomial formula [11]

$$f_\mathrm{A}(x) = h_n x^n + h_{n-1} x^{n-1} + \cdots + h x + h_0. \qquad (14)$$

The phase characteristic curves can be fitted by

$$f_\theta(x) = q_m x^m + q_{m-1} x^{m-1} + \cdots + q x + q_0. \qquad (15)$$

The amplitude ($f_\mathrm{A}(|V_\mathrm{LLRF}|)$) and phase ($f_\theta(|V_\mathrm{LLRF}|)$) of the SSA output can be calibrated using Eqs. (14) and (15), as shown in Fig. 9.

Furthermore, $f_\mathrm{A}(|V_\mathrm{LLRF}|)$ and $f_\theta(|V_\mathrm{LLRF}|)$ can also be estimated using the differential near the operating point. If the SSA is linear, its output amplitude increases linearly as the input amplitude increases, and the linear gain is $K = y/x$. In fact, the output amplitude of the SSA is often nonlinear with respect to the input amplitude; thus, the differential at point P is approximately $G = \Delta y/\Delta x$, as illustrated in Fig. 9 [11–13]. The amplitude variation of the SSA output signal depends on the value of G/K. For $G/K > 1$, the amplitude fluctuation of the LLRF output will be G/K times larger than that of the SSA. By contrast, for $G/K < 1$, the amplitude fluctuation of the LLRF output will be G/K times smaller than that of the SSA. We can see from Fig. 10 that the value of G/K is approximately 1.8; thus, a 1% fluctuation in the LLRF output amplitude near the operating point corresponds to a 1.8% fluctuation in the SSA output amplitude. It is easy to see that the ratio of the LLRF output amplitude and f_A is in good agreement with the value of G/K in Fig. 9. In addition, a 1% fluctuation in the LLRF output amplitude near the operating point will result in an error of $0.015°$ in the SSA output phase, according to the phase curves in Fig. 9. Noise from various sources also contributes to the error, which is difficult to determine from the LLRF output phase, as shown in Fig. 9. Thus far, we have estimated the amplitude and phase at point B (f_A and f_θ) successfully. Figure 9 shows that f_A and f_θ differ greatly in amplitude and phase (especially in phase) from V_f^*. Thus, we deduce that the nonlinearity of the SSA is not the main reason for the disagreement in phase by comparing the phase curves of $f_\theta(|V_\mathrm{LLRF}|)$ and f_A.

To determine whether the V_r signal is coupled with the V_f signal, it is necessary to calculate the actual V_f value of CM_{3-5}. The values of the complex constants a and b must be known before this calculation can be performed. The exact value of a for CM_{3-5} was obtained by theoretical analysis and derivation in Sect. III. The exact value of b can then be calculated using Eq. (9). From the known a and b values, the actual cavity forward signal can be calibrated using the measured signals V_r^* and V_f^*. Figure 11 shows the actual V_f signal, measured V_f signal, and SSA output signal considering the effects of the nonlinearity of the SSA. Panels (a), (b), and (c) represent the measurement results using the same calibration factors (i.e., a and b) but for different dates. The red lines represent the amplitude and phase of the SSA output signal considering the effect of the nonlinearity of the SSA. The blue lines show the calibrated actual forward signal, which represents V_f2 in the figure. The aqua lines represent the measured forward signal, as in the previous section, which represents V_f1. Figure 11(a) shows good phase agreement between the blue and red lines. The LLRF output phase is in agreement with the phase of the V_f signal in theory. This result confirms that the V_r signal is coupled with the V_f signal in the signal measurement. It is demonstrated that crosstalk in the measurement channels (e.g., crosstalk caused by the limited directivity of the directional coupler) is the major reason for the inaccurate measurement of V_f, and thus the phase discrepancy.

To further confirm the results of V_f signal calibration, we used the same calibration array (that is, the same values of
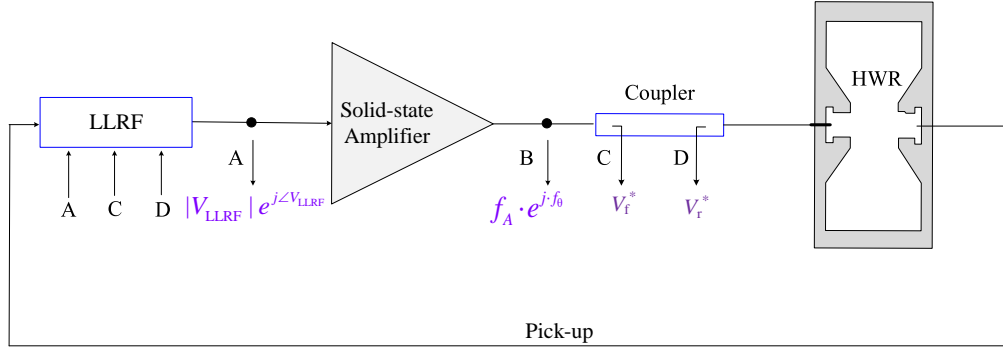
Fig. 8. Diagram of signal measurement. Points A and B represent the LLRF and SSA output signals, respectively. Points C and D represent the measured values of the cavity forward and reflected signals (V_f^* and V_r^*), respectively.
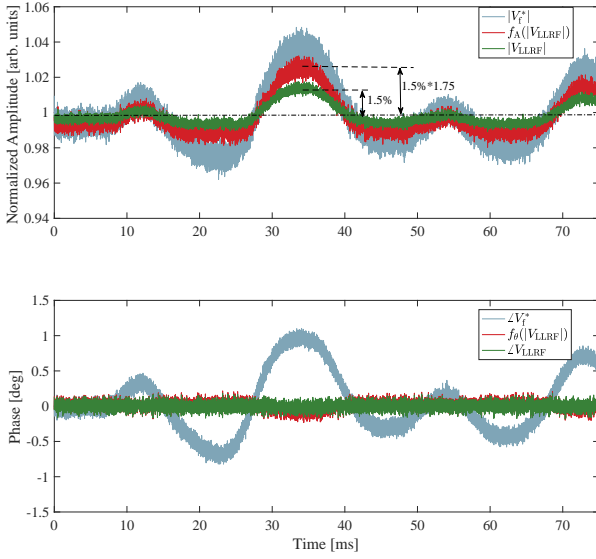

Fig. 9. (Color online) Amplitude and phase of LLRF output signal, which corresponds to point A in Fig. 8 (green, V_{LLRF}), SSA output signal considering the effect of SSA nonlinearity, which corresponds to point B in in Fig. 8 (red), and forward signal of measured corresponds to V_f^* (aqua). When the nonlinearity of the SSA is taken into account, the phases at point B ($f_\theta(|V_{LLRF}|)$) and point A ($\angle V_f^*$) still differ greatly.
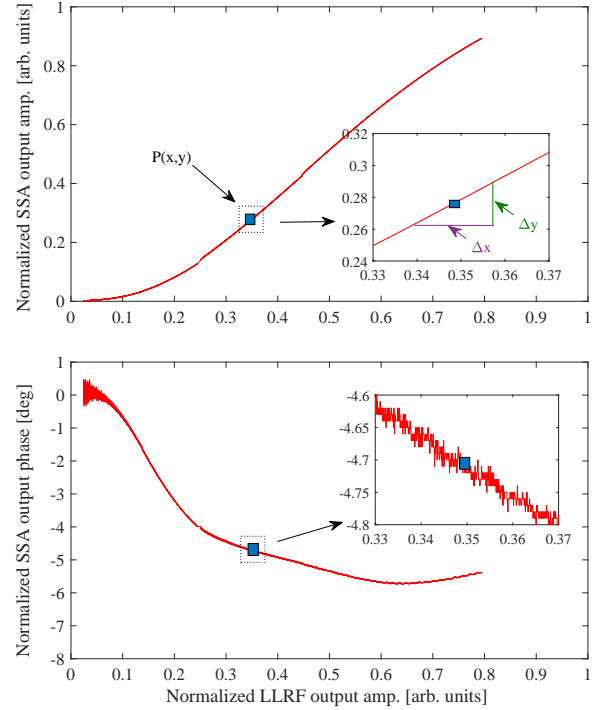

Fig. 10. (Color online) Schematic of amplitude and phase characteristics of SSA. The SSA and LLRF output amplitudes are normalized to the saturation point of the SSA.

a, b, c, and d) to calibrate the measurement results for other cases. In these cases, the working point of the SSA is the same as the working point in Fig. 10. The blue and red lines show good agreement [see Fig. 11(b) and 11(c)] in all cases, indicating that the calibration array has high universality.

B. Experimental result at KEK-cERL

The cERL facility was constructed at KEK to accommodate industrial applications of SC technology. It is a 1.3 GHz SC machine operated in CW mode [14–16]. At cERL, two nine-cell cavities (ML1 and ML2) with high Q_L values of up

to 1×10^7 were installed in the main linac.

At cERL, we observed that the LFD calculated using V_f differs from the theoretical value at the beginning of cavity filling in ML2. The discrepancy was assumed to be related to the inaccuracy of the V_f measurement due to signal crosstalk between the measurement channels. To verify the correctness of this assumption, the experimental data were re-analyzed. The cavity detuning ($\Delta\omega$) during the RF pulse without the beam can be estimated using the cavity differential equation
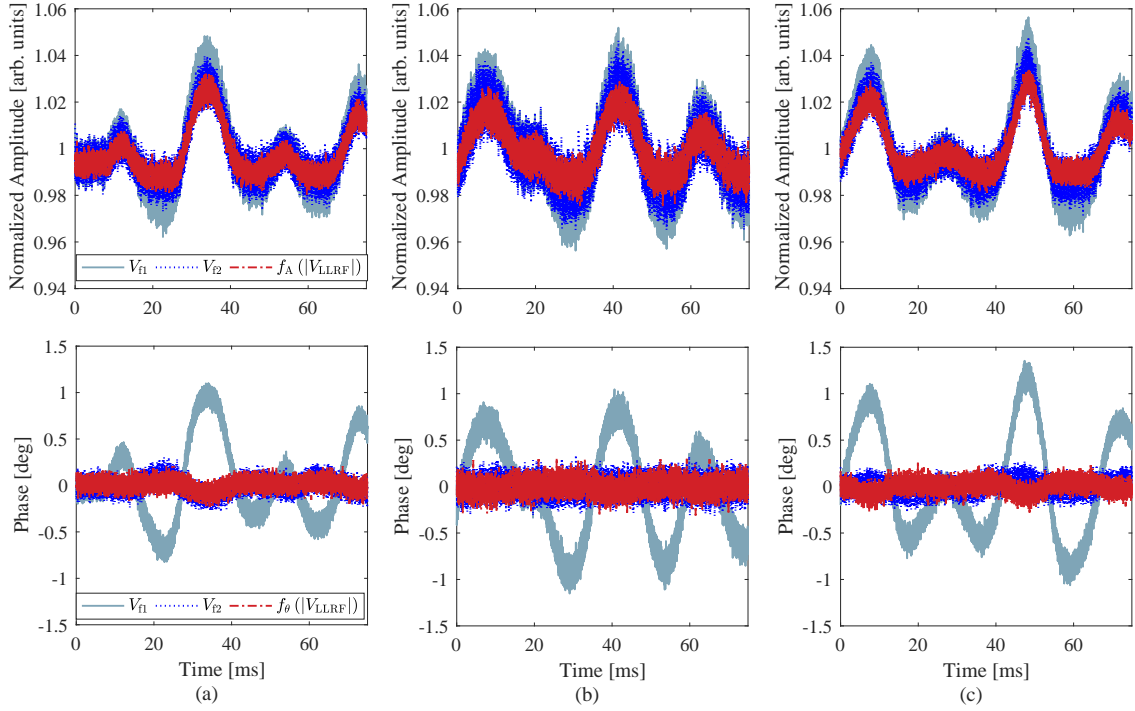
Fig. 11. (Color online) Amplitude and phase of SSA output signal considering the effects of the nonlinearity of the SSA (red), V_{f2} (the actual forward signal, blue), V_{f1} (the measured forward signal, aqua). Panels (a), (b) and (c) show the measurement results obtained using the same calibration factors a and b but for different dates. These cases show good phase consistency between the blue and red lines.

[7, 8, 12]

$$\Delta\omega = \frac{d\phi}{dt} - \frac{\omega_{0.5}(|2V_f|)\sin(\theta - \phi)}{|V_c|}, \qquad (16)$$

where ϕ and θ represent the phases of V_c and V_f, respectively. The quantity $\omega_{0.5}$ represents the cavity half-bandwidth. The detuning calculated using Eq. (16) includes other sources of detuning in addition to the LFD, although the LFD plays a major role in the overall detuning when the SC cavity is operated in pulse mode.

Moreover, for a given pulse pattern, the LFD can be calibrated using the LFD transfer function model $K(s)$ [7, 17–19] as

$$\Delta\omega_{LFD} = -2\pi K(s)E_{acc}^2, \qquad (17)$$

where $K(s)$ is the LFD transfer function, and E_{acc} is the accelerating gradient. The detuning at the beginning of the filling time can be estimated using the above equation [see Δf_{model} in Fig. 12(b)].

According to Eq. (16), the amplitude and phase ($|V_f|$ and θ, respectively) of V_f are required to calculate the cavity detuning $\Delta\omega$. When the crosstalk components b and c are not considered, the calibrated cavity forward signal V_f is equal to XV_f^* [Cali1 in Fig. 12(a)]. Under this assumption, the detuning Δf_{Cali1} is calibrated as shown in Fig. 12(b). Note that in Fig. 12(a), the amplitude of the Cali1 curve does not decrease to zero immediately when the RF power is switched off. As

shown in Fig. 12(b), the waveforms of Δf_{Cail1} and Δf_{model} (red curve) are slightly different at the beginning of the filling time.

Next, the crosstalk coefficients b and c in Eq. (2) are considered, and the coefficients a, b, c, and d are recalculated using the method described in Sec. III. Then, the actual cavity forward signal V_f is calibrated by $V_f = aV_f^* + bV_r^*$ [Cali2 in Fig. 12(a)]. As shown in Fig. 12(a), the amplitude of the Cali2 curve decreases to zero immediately when the RF power is turned off. Using the waveform of V_f in the cali2 curve, the LFD (Δf_{Cail2}) is obtained, as shown in Fig. 12(b). As expected, the trends of Δf_{Cail2} and Δf_{model} are in good agreement at the beginning of the filling time.

From the analysis above, we conclude that the inaccurate measurement of V_f can result in the miscalculation of the LFD. In addition, the analysis demonstrates the validity of the method of Brandt.

V. FUTURE WORK

In the future, after estimating the values of a, b, c, and d in the offline state, we will implement Eq. (2) in the FPGA. The actual cavity forward signal V_f and the actual reflected signal V_r are expected to be calibrated in real time. In the next stage, the calibrated V_f can be used to calibrate other parameters such as the cavity detuning and beam current.

In addition, the directivity of the directional coupler is related to its input power (the output of the RF source); there-
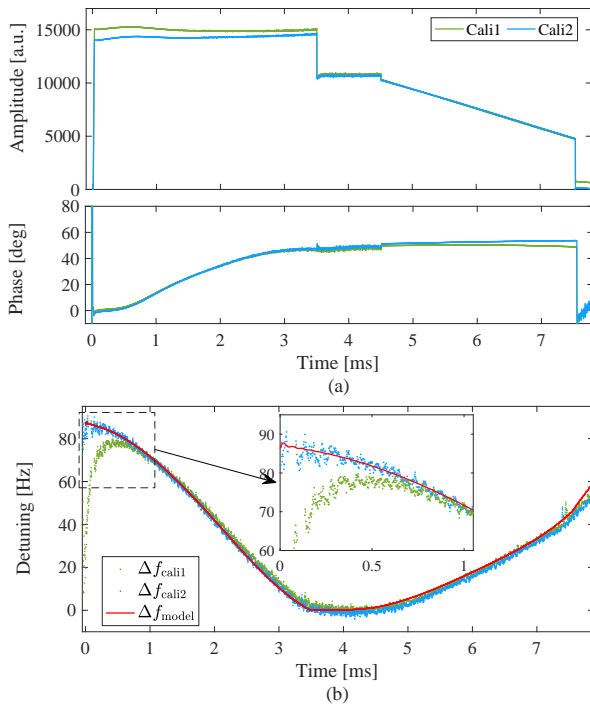
Fig. 12. (Color online) (a) Two methods of calibrating the actual cavity forward signal. Green line, Cali1: calibration of V_f without considering signal crosstalk. Blue line, Cali2: calibration of V_f considering signal crosstalk. (b) Comparison of LFD calculated using Eq. (16) without considering signal crosstalk (green), using Eq. (16) considering signal crosstalk (blue), and using Eq. (17) (red).

fore, the value of a/X may also depend on the location of the nonlinear operating point of the SSA. In the next step, we will attempt to determine the dependence of the parameter a/X on the operation point of the RF source. This research will be based on many measurements and calculations at CAFe at various SSA powers according to the research purpose.

Finally, this paper assumes that crosstalk exists only between the measured forward and reflected waves. However, RF components could also contribute to the crosstalk signal. We will study these crosstalk relationships further in future work.

VI. SUMMARY

In this study, the actual V_f was successfully calibrated using the method proposed by Brandt. We verified the validity of this method for the CAFe and cERL facilities. The study at CAFe indicated that inaccurate V_f measurement is caused mainly by the directivity of the couplers. We confirmed that at cERL, the calibration accuracy of the cavity detuning can be significantly improved by considering the crosstalk components resulting from, for example, the limited directivity of the directional coupler.

ACKNOWLEDGMENTS

AUTHOR CONTRIBUTIONS

All authors contributed to the study conception and design. Material preparation, data collection and analysis were performed by Feng Qiu, Jin-Ying Ma and Gui-Rong Huang. The first draft of the manuscript was written by Jin-Ying Ma and all authors commented on previous versions of the manuscript. All authors read and approved the final manuscript.

[1] Y. He, T. Tan, A.D. Wu et al., Operation Experience at CAFe. *in Oral presentation of the 2021 International Conference on RF Superconductivity (SRF'21)*, virtual conference, (JACoW, virtual conference, 2021). Available at https://indico.frib.msu.edu/event/38/attachments/160/1298/MOOFAV03_yuan_he.pdf.

[2] S.H. Liu, Z.J. Wang, H. Jia et al., Physics design of the CIADS 25 MeV demo facility. Nucl. Instrum. Meth. A. 843, 11–17 (2017). doi:10.1016/j.nima.2016.10.055

[3] Q. Chen, Z. Gao, Z.L. Zhu et al., Multi-frequency point supported LLRF front-end for CiADS wide-bandwidth application. Nucl. Sci. Tech. 31(3), 29 (2020). doi:10.1007/s41365-020-0733-9

[4] F. Qiu, S. Michizono, T. Matsumoto et al., Combined disturbance-observer-based control and iterative learning control design for pulsed superconducting radio frequency cavities. Nucl. Sci. Tech. 32(6), 56 (2021). doi:10.1007/s41365-021-00894-y

[5] M. Omet, A. Kuramoto, T. Matsumoto et al., Development and application of a frequency scan-based and a beam-based calibration method for the llrf systems at KEK STF. in *Proceedings of the 9th Annual Meeting of Particle Accelerator Society of Japan (PASJ2015)*, Osaka, Japan, 2012. Available at https://www.pasj.jp/web_publish/pasj9/proceedings/PDF/FRLR/FRLR09.pdf

[6] R. Kalt, Z.Q. Geng, RF and beam stability at Swiss-FEL, *in Oral presentation of the LLRF Workshop 2019*, Chicago, USA September 29 – October 3, 2019. Available at https://indico.fnal.gov/event/21836/contributions/64989/attachments/40775/49374/RF_and_beam_stability_at_SwissFEL.pdf

[7] F. Qiu, T. Miura, D. Arakawa et al., RF commissioning of the compact energy recovery linac superconducting cavities in pulse mode. Nucl. Instrum. Meth. A. 985, 164660 (2021). doi:10.1016/j.nima.2020.164660

[8] B. Alexander, Development of a finite state machine for the automated operation of the LLRF control at FLASH. Ph.D. thesis, Universitt Hamburg, 2007.

[9] M. Grecki, S. Pfeiffer, Resonance control of superconducting cavities at heavy beam loading conditions. in *Proceeding of IPAC2012*, New Orleans, Louisiana, USA. doi:10.1103/PhysRevAccelBeams.21.032003

[10] F. Qiu, S. Michizono, T. Matsumoto et al., Real-time cavity simulator-based low-level radio-frequency test bench and applications for accelerators. Phys. Rev. Accel. Beams 21, 032003 (2018). doi:10.1103/PhysRevAccelBeams.21.032003

[11] M. omet, S. Michizono, T. Miura et al., FPGA-based klystron linearization implementations in scope of ILC. Nucl. Instrum. Meth. A. 768, 69–76 (2014). doi:10.1016/j.nima.2014.09.007

[12] F. Qiu, Z.L. Zhu, J,Y. Ma et al., An approach to characterize Lorentz force transfer function for superconducting cavities. Nucl. Instrum. Meth. A. 1012, 165633 (2021). doi:10.1016/j.nima.2021.165633

[13] L.P. Sun, Z.Y. Yuan, C. Zhang et al., New thermal optimization scheme of power module in solid-state amplifier. Nucl. Sci. Tech. 30(4), 68 (2019). doi:10.1007/s41365-019-0585-3

[14] M. Akemoto D. Arakawaet, S. Asaokaal et al., Construction and commissioning of the compact energy-recovery linac at KEK. Nucl. Instrum. Meth. A. 877, 197–219 (2018). doi:10.1016/j.nima.2017.08.051

[15] Y. Morikawa, K. Haga, M. Hagiwara et al., New Industrial application beam-line for the cERL in KEK, in *Proceedings of the 10th International Particle Accelerator Conference*, Melbourne, Australia, 2019. https://doi.org/10.18429/JACoW-IPAC2019-THPMP012

[16] F. Qiu, T. Miura, D. Arakawa et al., Application of disturbance observer-based control on pulsed superconducting radio frequency cavities. Phys. Rev. Accel. Beams 24(1), 012804 (2021). doi:10.1103/PhysRevAccelBeams.24.012804

[17] R.R. Mitchell, K.Y. Matsumoto, G. Ciovati et al., Lorentz Force Detuning analysis of the spallation neutron source (SNS) accelerating cavities, in *10th Workshop on RF Superconductivity*, Tsukuba City, Japan, 2001. Available at https://digital.library.unt.edu/ark:/67531/metadc723708/m2/1/high_res_d/786098.pdf

[18] T. Schilcher, Ph.D. thesis, University Hamburg, 1998.

[19] J.Y. Ma, G.R. Huang, Z.Gao et al., The resonant frequency measurement method for superconducting cavity with Lorentz force detuning. Nucl. Instrum. Meth. A. 993(5),165085 (2021). doi:10.1016/j.nima.2021.165085